# A Multi-chain Surrogate-assisted Hybrid Optimization Framework for Joint Identification of Groundwater Contaminant Sources and Hydrogeological Parameters

Mengtian Wu[1,2,3], Xuan Huang[4], Pengcheng Xu[5], Han Chen[6], Xu Yang[6], Jin Xu[6], Qingyun Duan[1,2,3]

[1] National Key Laboratory of Water Disaster Prevention, Hohai University, Nanjing, China
[2] College of Hydrology and Water Resources, Hohai University, Nanjing, China
[3] China Meteorological Administration Hydro-Meteorology Key Laboratory, Hohai University, Nanjing, China
[4] Key Laboratory of Taihu Basin Water Resources Research and Management of Ministry of Water Resources, Nanjing Hydraulic Research Institute, Nanjing, China
[5] Macau Environmental Research Institute, Faculty of Innovation Engineering, Macau University of Science and Technology, Macau, China
[6] State Key Laboratory of Water Cycle and Water Security, College of Water Conservancy and Hydropower Engineering, Hohai University, Nanjing, China

*Correspondence to*: Qingyun Duan (qyduan@hhu.edu.cn)

Deleted: Yang

Deleted: Xu

**Abstract.** Rapid and accurate identification of groundwater contaminant information and hydrogeological parameters is crucial for effective groundwater remediation and risk management. Within a simulation-optimization framework, this task is inherently posed as a mixed-variable optimization problem involving discrete parameters (e.g., source locations) and continuous ones (e.g., hydraulic heads, conductivities, and release fluxes). However, several challenges arise in this context. First, conventional optimization algorithms often exhibit slow convergence and unstable performance. Second, they typically require thousands of simulations to adequately explore the complex parameter space, resulting in prohibitive computational costs. To address these issues, this study develops a surrogate-assisted hybrid algorithm that integrates the Cooperative Search Algorithm (CSA) and Tabu Search (TS) within a synergistic multi-chain optimization framework, termed SA-CSA-TS. In each iteration, individual chains first perform independent CSA-based optimization to promote broad global exploration, after which they collaboratively refine source locations through a neighbourhood search guided by a shared tabu list. In addition, surrogate models equipped with a reconstruction strategy partially replace groundwater simulations, thereby substantially reducing the computational burden. Case studies reveal that the Radial Basis Function (RBF) outperforms other mainstream surrogate models in both accuracy and stability. Furthermore, comparative experiments confirm that the proposed SA-CSA-TS framework not only achieves higher solution accuracy but also significantly reduces computational demand, demonstrating strong potential for efficient groundwater contamination diagnosis.

## 1 Introduction

Groundwater contamination has become an increasingly critical issue, posing significant risks to environmental safety and public health (Gorelick and Zheng, 2015; Li et al., 2021a; Agbotui et al. 2025). Effective groundwater remediation requires rapid and accurate identification of contaminant source parameters (Bai and Tahmasebi, 2022; Mahar and Datta, 2001; Zhao et al., 2016). However, due to the invisibility of groundwater systems and sparse monitoring (Mirghani et al., 2009), source information cannot always be obtained directly. Instead, it must be inferred from observations, typically within a simulation-optimization (S-O) framework (Singh, 2015).

Within the S-O framework, simulation models such as MODFLOW, MT3DMS, and FEFLOW are employed to describe the spatial and temporal evolution of contaminant plumes (Delshad et al., 1996; Harbaugh, 2005; Zheng and Wang, 1999). The quality of candidate parameter sets is evaluated through performance metrics (e.g., NSE and RMSE) that measure the discrepancy between simulated and observed data. Optimization algorithms then iteratively adjust these parameters to minimize the selected metrics, thereby identifying the most probable parameter values. Common algorithms, including Genetic Algorithm (GA) (Ayvaz and Elci, 2018; Singh and Datta, 2006), Particle Swarm Optimization (PSO) (Meenal and Eldho, 2012; Pan et al., 2023), and Simulated Annealing (Jha and Datta, 2013), have demonstrated considerable success in groundwater contamination source identification (GCSI) (Swetha et al., 2025). Consequently, the S-O framework incorporating these groundwater models and algorithms has been widely adopted in groundwater contamination studies (Guneshwor et al., 2018).

Despite these advantages, the S-O framework still faces several challenges that hinder its accuracy and computational efficiency (Wu et al., 2022b). For instance, real-world GCSI often requires identifying source locations, which inherently transforms the task into a mixed-variable problem (Li et al., 2023). Such problems involve the simultaneous estimation of both discrete parameters (e.g., source locations) and continuous parameters (e.g., time-dependent contaminant release rates) (Wang et al., 2024). However, many existing optimization algorithms handle discrete variables through simple conversion techniques, such as binary encoding, grid-based discretization, or rounding schemes. These treatments can introduce approximation errors or impose artificial constraints, ultimately reducing solution quality. In addition, the mixed-variable structure produces highly complex, discontinuous, and multimodal objective landscapes. As a result, algorithms are more likely to converge prematurely to local optima (Chang et al., 2021).

For these reasons, some studies have introduced new or hybrid algorithms. For instance, Flying Foxes Optimization (FFO) has demonstrated superior search efficiency and accuracy in groundwater problems (Li et al., 2023). Similarly, the hybrid GA-PSO algorithm (Wang et al., 2015) improves performance by combining the global exploration capabilities of GA with the fast convergence of PSO, while Li et al. (2021b) also propose a Hybrid Homotopy-Genetic Algorithm. However, most of these approaches adopt a simultaneous optimization strategy that treats source locations and release rates as equivalent variables. In practice, this assumption oversimplifies the physical reality of groundwater transport. Source locations typically exert a dominant influence because they determine the transport pathways and the geometry of the plume. In contrast, release rates

Deleted: ).

and hydrogeological parameters mainly scale the concentration magnitudes. This sensitivity disparity creates a multimodal response surface, where multiple location combinations can reproduce sparse field observations with similar accuracy. This characteristic significantly increases the risk of premature convergence and may lead to the misidentification of critical source information.

The computational burden associated with GCSI cannot be ignored, as optimization algorithms often require thousands of simulations to adequately explore the parameter space (Asher et al., 2015; Ouyang et al., 2017). This intensive demand severely limits practical applications, particularly for complex or large-scale groundwater simulation models (Song et al., 2019). In this context, surrogate modelling, as a data-driven technique, has become a widely adopted choice (Song et al., 2018). By approximating the behaviour of high-fidelity groundwater models, surrogate models can enable more efficient and feasible source identification. Common surrogate models include Kriging, Gaussian Process (GP) (Rasmussen and Williams, 2006), Support Vector Regression (SVR) (Chang and Lin, 2011), Radial Basis Function (RBF) (Broomhead and Lowe, 1988), and ensembles of these models (Xing et al., 2019; Yin and Tsai, 2020; Zhu et al., 2024). However, most existing studies still select surrogate models based primarily on empirical preference, and few have systematically evaluated or compared their performance and suitability for groundwater systems (Hou and Lu, 2018; Wu et al., 2022a; Luo et al., 2025). To address this gap, the present study conducts a comprehensive comparison of mainstream surrogate models and identifies the most effective one for GCSI.

Overall, this study proposes a multi-chain surrogate-assisted hybrid optimization framework, termed SA-CSA-TS. The framework adopts a multi-chain structure operating across two distinct optimization stages. In the first stage, individual chains execute CSA-based optimization to enhance global exploration, with well-trained surrogate models replacing time-consuming groundwater simulations. In the second stage, chains collaboratively refine source locations through a neighbourhood search guided by a shared tabu list. This cooperative strategy enables efficient identification of source positions that control the contaminant plume distribution. To support the framework, several surrogate models are evaluated, and the RBF model is found to provide the most accurate approximation for groundwater applications. Case studies show that SA-CSA-TS can reduce computational cost by up to 85-88% while achieving higher identification accuracy than conventional algorithms. These results demonstrate the efficiency and reliability of the proposed framework and offer valuable insights for groundwater contamination remediation.

## 2 Methodology

### 2.1 Groundwater simulation

For groundwater contamination source identification (GCSI), this study adopts a simulation-optimization framework (Mahar and Datta, 2001). There are various effective simulation techniques available for groundwater modelling. In this study, MODFLOW 6 (Hughes et al., 2017) is adopted to simulate groundwater flow and pollutant transport, facilitated by the Python package FloPy (Bakker et al., 2016), which provides a convenient and flexible interface for model construction and execution. The governing partial differential equation for transient flow in a two-dimensional aquifer system can be given as follows:

$$\frac{\partial}{\partial x_i}\left(K_{i,j}\frac{\partial h}{\partial x_j}\right) + W = S_s\frac{\partial h}{\partial t} \quad (1)$$

where $K_{i,j}$ denotes the hydraulic conductivity, $m \cdot d^{-1}$; $h$ denotes the hydraulic head, $m$; $x_i$ and $x_j$ are the coordinates along the axis, $m$; $S_s$ is the specific storage of the porous material; and $W$ is the volumetric flux per unit area.

Solute transport can be described by the following advection-dispersion-reaction equation under known hydrogeological conditions:

$$\frac{\partial}{\partial x_i}\left(\theta D_{ij}\frac{\partial C^k}{\partial x_j}\right) - \frac{\partial}{\partial x_i}(\theta v_i C^k) + q_s C_k^s + \sum R_n = \frac{\partial(\theta C^k)}{\partial t} \quad (2)$$

where $\theta$ is effective porosity; $C^k$ is the dissolved concentration of the species $k$, $mg \cdot L^{-1}$; $D_{i,j}$ is the dispersion coefficient tensor, $m^2 \cdot d^{-1}$; $v_i$ is the linear pore water velocity, $m \cdot d^{-1}$; $q_s$ is the volumetric flow rate per unit volume, representing sources or sinks; $C_k^s$ is the source or sink concentration of species $k$, $mg \cdot L^{-1}$; $R_n$ is the chemical reaction term, $mg \cdot L^{-1} \cdot d^{-1}$.

### 2.2 UQPyL

UQPyL [1] is a Python package developed by our team to support uncertainty quantification and optimization in computational modelling. The package integrates a comprehensive set of tools, including sampling techniques, surrogate modelling, parameter analysis methods, and global as well as hybrid optimization algorithms. Its modular and extensible design enables users to flexibly combine different components, facilitating rapid prototyping and testing of new algorithms. Moreover, UQPyL includes a default interface to couple external numerical simulators, making it suitable for computationally intensive applications such as groundwater modelling. In this study, UQPyL provides the foundation for implementing the proposed SA-CSA-TS algorithm, conducting surrogate-model comparison experiments, and ensuring a consistent environment for benchmarking different optimization methods.

[1] www.uq-pyl.com



Formatted: Space Before: 12 pt

Deleted: For GCSI, this study adopts a simulation-optimization framework (Mahar and Datta, 2001). In this framework, the simulation model describes the spatial and temporal evolution of contaminants under specified input parameters, while the optimization algorithm iteratively refines these inputs to minimize the discrepancy between observed and simulated concentrations. Building on this concept, we develop a multi-chain surrogate-based optimization algorithm, SA-CSA-TS, which synergizes the Cooperative Search Algorithm (CSA) and Tabu Search (TS). The following sections first introduce the groundwater model used in this study and then describe the implementation and components of SA-CSA-TS.¶
**2.1 Simulation¶**

Deleted: It is worth noting that although MODFLOW 6 is used here, the simulation-optimization framework is versatile and applicable to other groundwater models.¶

Deleted: **Optimization¶**
**2.2.1**

## 2.3 Overview of the proposed algorithm

This study develops a surrogate-assisted hybrid optimization algorithm, SA-CSA-TS, built upon a multi-chain framework in which each chain iteratively performs a two-stage search. Global exploration is conducted using the Cooperative Search Algorithm (CSA), followed by local refinement using Tabu Search (TS). To reduce dependence on computationally expensive groundwater simulations, surrogate models with dynamic reconstruction are embedded into both stages. In addition, designed inter-chain communication enables the exchange of evaluated samples, enhancing data diversity and improving surrogate accuracy.

Figure 1 illustrates the overall workflow. The process begins with initial sampling, and the groundwater model is used to evaluate these samples to initialize the chain archive $D$. After that, the algorithm enters the multi-chain optimization phase.

During each iteration, surrogate models are at first constructed. The key feature is synergistic learning, where each chain builds its surrogates not only from its own history but also from the evaluated solutions shared by other chains (see the red arrows in Fig. 1). In the first stage, each chain independently performs CSA under the guidance of surrogates to explore the global search space. The best individual from each chain is then evaluated using the groundwater simulator and used to update $D$. Local refinement is performed in the second stage. Before activating TS, the surrogate models are reconstructed using all newly obtained evaluations. TS subsequently explores neighbourhood solutions through multiple-move operators, and cooperation among chains is realized via a shared tabu list, which prevents redundant searches and promotes effective diversification. Surrogates continue to pre-screen candidate solutions, and only the most promising candidate from each chain is evaluated with the groundwater model. This iterative process continues until the predefined maximum evaluations of groundwater model $FE_{max}$ is reached.

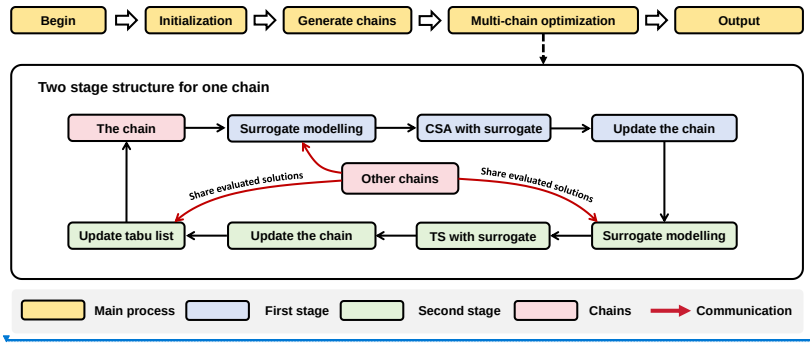


**Figure 1.** Overall framework of SA-CSA-TS.

In summary, SA-CSA-TS enhances GCSI efficiency through three integrated mechanisms. First, the multi-chain framework enables synergistic learning by sharing evaluated information across chains. Second, the sequential deployment of CSA and TS provides a strong balance between global exploration and local intensification. Finally, surrogate models with



**Deleted:** 2.2 Cooperative Search Algorithm¶
The Cooperative Search Algorithm (CSA) is a population-based optimization method inspired by cooperative behaviours observed in social systems (Feng et al., 2021). CSA emphasizes team communication, reflective learning and internal competition among individuals. These mechanisms enable the algorithm to maintain diversity and accelerate convergence, making it suitable for solving high-dimensional, nonlinear, and multimodal problems. In CSA, a population

**Formatted:** Heading 2

**Deleted:** algorithms

**Deleted:** candidate solutions $\{x_i\}_{i=1}^{N}$ is initially generated. During the optimization process, individuals improve their positions by learning from others within the population. For example, at iteration $t$, the update of the $i$-th individual typically follows a team communication rule: ¶

$$u_i^{t+1} = x_i^t + A_i^t + B_i^t + C_i^t \quad (3)$$¶

$$A_i^t = log\left(1/\phi(0,1)\right) \cdot (g_{ind}^t - x_i^t)$$¶

$$B_i^t = \alpha \cdot \phi(0,1) \cdot (gm^t - x_i^t)$$¶

$$C_i^t = \beta \cdot \phi(0,1) \cdot (pm^t - x_i^t)$$¶

where $A_i^t$, $B_i^t$ and $C_i^t$ denote the knowledge components from the chairman, board of directors, and board of supervisors, respectively. $g_{ind}^t$ is the $ind$-th global best individual at iteration $t$. The $gm^t$ represents the mean position of the top $M$ global best individuals. The $pm^t$ is the mean position of the $i$th personal best individual.¶
In addition, the individual is also updated by summing its own experience in its opposite direction, which can be expressed as follows:¶

$$v_{i,j}^{t+1} = \begin{cases} r_{i,j}^{t+1} \; if\left(u_{i,j}^{k+1} \geq c_j\right) \\ p_{i,j}^{t+1} \; if\left(u_{i,j}^{k+1} < c_j\right) \end{cases}$$¶

$$r_{i,j}^{t+1} = \begin{cases} \phi(ub_j + lb_j - u_{i,j}^{t+1}, c_j) & if\left(|u_{i,j}^{t+1} - c_j| < \phi(0,1) \cdot |ub_j - lb_j|\right) \\ \phi(lb_j, ub_j + lb_j - u_{i,j}^{t+1}) & otherwise \end{cases}$$
(4)¶

...

**Deleted:** 3.1 Overview¶

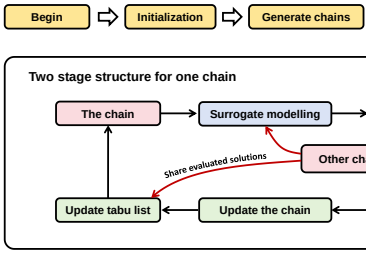


**Deleted:**

**Deleted:** :

**Formatted:** Font: Not Bold

dynamic reconstruction reduce computational burden while preserving high-fidelity prediction accuracy to guide the search effectively.

For clarity, the pseudocode of SA-CSA-TS is also provided:

**Algorithm 1**: SA-CSA-TS

**Input:** The maximum number of high-fidelity evaluations $FE_{max}$; The number of initial samples $N_I$; The number of chains $K$.
**Output:** The best optimal solution $best$.
**01:** Initialize $FE \leftarrow 0$; $T \leftarrow \emptyset$; $D \leftarrow \emptyset$; /* $T$: tabu list, $D$: chain archive */
**02:** Initialize $N_I$ by Latin Hypercube Sampling
**03:** $S \leftarrow$ evaluated by the groundwater model and distributed evenly into $D$
**04:** $FE \leftarrow FE + N_I$
**05: while** $FE < FE_{max}$:
**06:** Construct the surrogate model $\tilde{F}$ with $D$
**07:** **For** each chain $k = 1$ to $K$: /*Enter the first stage*/
**08:** perform the cooperative search optimization using $\tilde{F}$ as the evaluator
**09:** **End For**
**10:** $S_1 \leftarrow$ Collect the best individual from each chain
**11:** Evaluate $S_1$ using the groundwater model; $D \leftarrow D \cup S_1$
**12:** Retrain the surrogate model $\tilde{F}$ with $D$
**13:** **For** each chain $k = 1$ to $K$: /* Enter the second stage */
**14:** TS operator using $\tilde{F}$ as the evaluator
**15:** **End For**
**16:** $S_2 \leftarrow$ Collect the best individual from each chain
**17:** Evaluate $S_2$ using the groundwater model; $D \leftarrow D \cup S_2$
**18:** $T \leftarrow$ update the tabu list based on $S_2$
**19:** $FE \leftarrow FE + 2 * K$
**20: End While**
**21:** $best \leftarrow$ update the best optimal solution from $D$
**22: Return** $best$

Deleted: 3.

## 2.4 Surrogate modelling in SA-CSA-TS

To alleviate the computational burden of repeated groundwater simulations, surrogate modelling is embedded into the proposed SA-CSA-TS framework. In GCSI, candidate parameters should be evaluated by the groundwater simulator to quantify the mismatch between simulated and observed concentrations at the monitoring wells. Since the optimization procedure requires a large number of candidate evaluations, direct reliance on the high-fidelity simulator becomes computationally expensive. To address this issue, SA-CSA-TS incorporates surrogate models as inexpensive approximators of the simulation-based objective, enabling rapid screening of candidate solutions while retaining the groundwater model for selected exact evaluations.

Formatted: Normal

Within the optimization-simulation framework, the quality of candidate parameters is evaluated by the groundwater model (see the dashed line of Fig. 2). However, the entire optimization process typically requires thousands of forward simulations. To alleviate the computational demand, the SA-CSA-TS incorporates a surrogate modelling technique (see the solid line of Fig. 2).

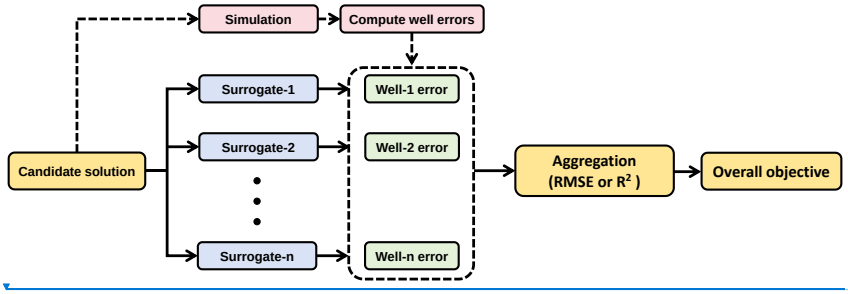


**Figure 2.** Workflow of solution evaluation with simulation or surrogate models.

As illustrated in Fig. 2, a set of surrogate models is constructed to estimate the discrepancy (e.g., $RMSE$ or $R^2$) between simulated and observed concentrations at each monitoring well. Therefore, the number of surrogate models equals the number of observation wells. During optimization, these surrogates substitute for repeated groundwater simulations and provide rapid approximations of the error. The predicted discrepancies across all wells are then aggregated, and their sum is adopted as the overall objective function, guiding the evaluation of candidate parameters and the subsequent optimization.

## 2.6 Global exploration via surrogate-assisted CSA

In SA-CSA-TS, the first stage focuses on global exploration, where each chain independently executes the Cooperative Search Algorithm (CSA) with the support of trained surrogate models. Fig. 3 illustrates the workflow of this surrogate-assisted CSA. Unlike the original CSA, the evaluation of individuals is performed using surrogate predictions instead of running computationally expensive groundwater simulations (the red dashed line of Fig. 3). Only the superior solutions produced in this stage are then used to update the chain's current position (Line 08 in Algorithm 1). Furthermore, this surrogate-assisted CSA module is implemented as a standalone benchmark algorithm, referred to as SA-CSA, enabling a direct comparison with the complete SA-CSA-TS to show the specific contributions of the multi-chain architecture and the Tabu Search.



Deleted:

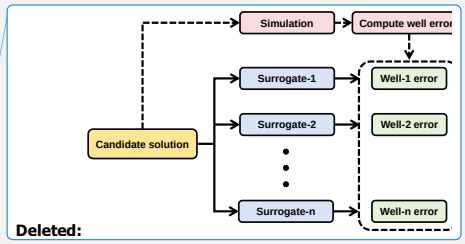


Deleted: :

Formatted: Font: Not Bold

Formatted: Font: Not Bold

Deleted: 3.3 Surrogate

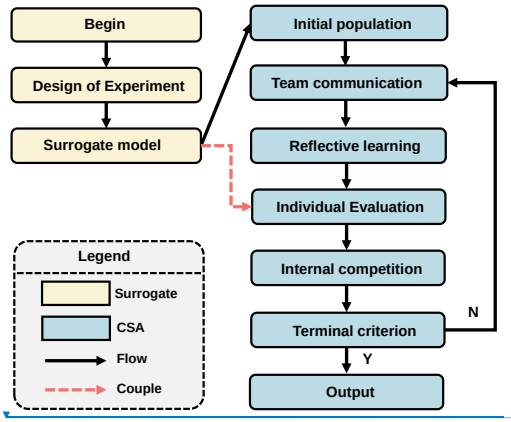


**Figure 3.** Workflow of surrogate-assisted CSA.

## 2.7 Local refinement via surrogate-assisted TS

Unlike the previous stage, where CSA operates independently in each chain, the Tabu Search (TS) stage is executed under a coordinated multi-chain framework. In this design, all chains share a common tabu list, which serves as a collective memory to prevent any chain from revisiting previously explored regions. Since the discrete variable corresponds to the index of a potential contamination-source area, the tabu list is defined over this finite set, and its maximum size is equal to the total number of candidate source areas. The corresponding search mechanism is illustrated in Fig. 4. Guided by the retrained surrogate model, each chain explores its neighbourhood to identify promising candidates. As shown, the search trajectories are strictly constrained by the shared history, enabling the algorithm to better navigate multi-modal landscapes. For example, moves that enter tabu-listed areas (highlighted by red arrows) are prohibited. After selecting the most promising solutions, the algorithm performs simulation-based evaluations and subsequently updates the shared tabu list, thereby allowing dynamic information exchange among all chains.

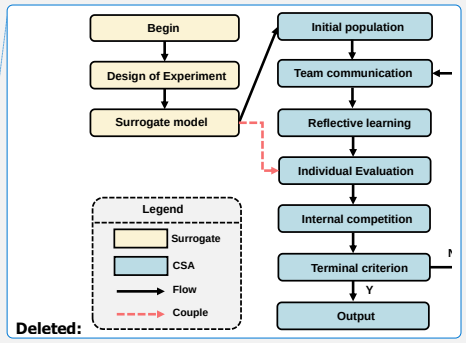


Deleted: :

Formatted: Font: Not Bold

Deleted: 3.4 Surrogate

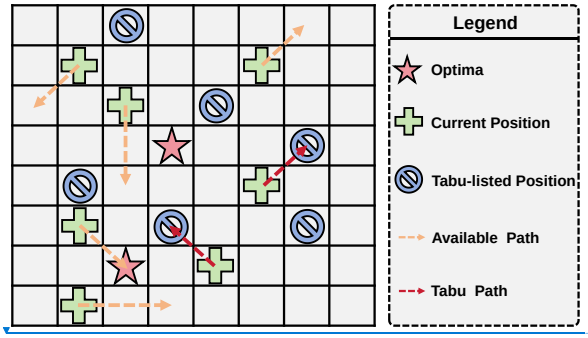


**Figure 4** Diagram of multi-chain Tabu Search.

We describe the rule for updating the tabu list. Let $x_i$ and $f_i$ denote the current solution and its objective value of the $i$-th chain, respectively, and let $f_{best}^i$ represent the historical best objective value recorded by that chain. The update mechanism consists of the following three cases:

If $f_i > f_{best}^i$, the discrete component of $x_i$, denoted $x_i^d$, is added to the tabu list $T$, preventing the algorithm from revisiting this configuration in subsequent iterations.

If $f_i < f_{best}^i$, and $x_i^d \in T$, the tabu status of $x_i^d$ is removed, allowing the algorithm to reconsider this configuration since a better solution has been found.

If $f_i < f_{best}^i$ and $x_i^d \notin T$, both the best solution $x_{best}$ and the best objective $f_{best}^i$ are updated accordingly.

## 4 Case studies

To comprehensively evaluate the performance of the proposed SA-CSA-TS algorithm, three case studies are conducted. Cases 1 and 2 are hypothetical scenarios designed to compare the effectiveness of different surrogate models and to enable an in-depth examination of the internal behaviour of SA-CSA-TS. Case 3 involves a practical engineering problem, suitable for validating the applicability and robustness of SA-CSA-TS in real-world conditions.

### 4.1 Case 1

The study area is a two-dimensional, homogeneous, anisotropic confined aquifer ($800\ m \times 1200\ m$), as illustrated in Fig. 5. The left and right boundaries are assigned constant hydraulic heads, and the remaining boundaries are treated as no-flow. For simulation, the domain is discretized into a grid of $16 \times 24$ cells, with a uniform cell size of $50\ m$. The basic hydrogeological parameters used in this case are summarized in Table 1.

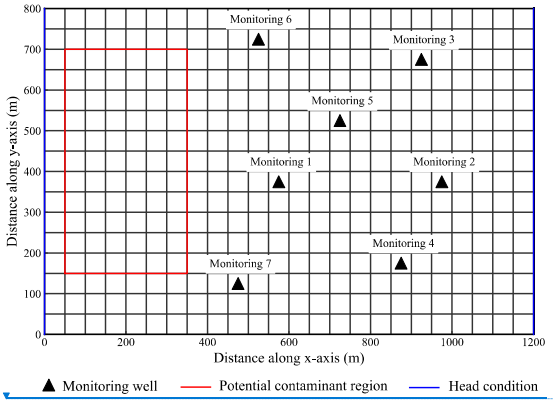


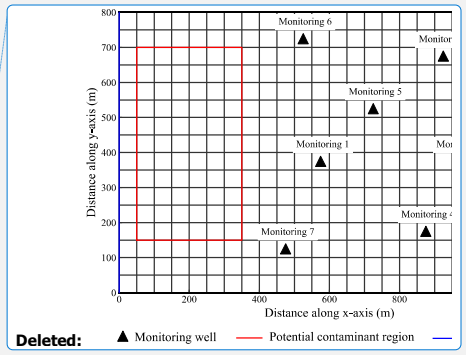


**Figure 5.** Schematic diagram in Case 1.

**Table 1.** Basic values and ranges of hydrogeological parameters in Case 1.

| Name | Value or range |
|---|---|
| Hydraulic conductivity, $K$, $m/day$ | $15.0 - 35.0$ |
| Porosity, $\theta$ | 0.25 |
| Longitudinal dispersity, $\alpha_L$, $m$ | 40.0 |
| Transverse dispersity, $\alpha_T$, $m$ | 15.0 |
| Saturated thickness, $b$, $m$ | 20.0 |
| Hydraulic head of the left boundary, $H_1$, $m$ | $40.0 - 50.0$ |
| Hydraulic head of the right boundary, $H_2$, $m$ | $30.0 - 40.0$ |

The potential contamination source zone, also shown in Fig. 5, represents an industrial area with intensive activities, where contaminants may be intermittently released into the aquifer. Within this zone, one or more contamination sources may exist. To capture solute transport behaviour and provide data for the inverse analysis, seven monitoring wells are distributed across the study area (the triangle in Fig. 5).

In Case 1, a single contaminant source is considered. The total simulation time is 40 months, divided into 20 stress periods (SPs), with the source releasing contaminants only during the first five SPs. The true source location and its release fluxes for these five SPs are listed in Table S1. The contaminant plume distributions at the 5th and 10th SPs are shown in Fig. 6.

For this case, the parameters to be identified include:

(a) Hydrogeological parameters: The hydraulic conductivity ($K$) and the boundary head ($H_1$ and $H_2$). Their ranges are listed in Table 1;

(b) Source-related parameters: The source locations ($SI$ and $SJ$, where $SI$ denotes the grid index in the $x$-direction and $SJ$ denotes the grid index in the $y$-direction, respectively) and their time-varying release fluxes ($S_iP_t$, where $i$ denotes the index of the source, $i = 1$; and $t$ denotes the index of the stress period, $t = 1$ to 5 ), with the value of each flux bounded between 0 and 100 $kg/day$.

Deleted: :

Formatted: Font: Not Bold

Formatted: Font: Not Bold

Deleted: :

Formatted: Font: Not Bold

Formatted: Font: Not Bold

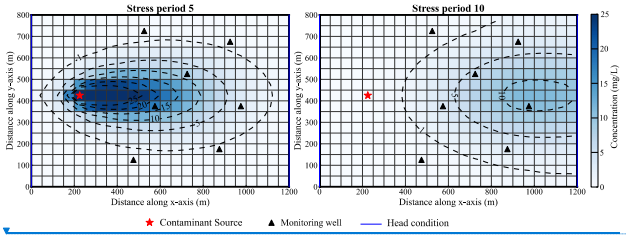


**Figure 6.** Distribution of contaminant plume in the 5th and 10th SPs of Case 1.

### 4.2 Case 2

Case 2 adopts the same hydrogeological setting and numerical configuration as Case 1, but involves a more complex contamination scenario. In this case, three independent contaminant sources are introduced within the potential source zone. Their true locations and time-varying release fluxes are summarized in Table S2. The contaminant plume distribution at the 5th and 10th SPs is illustrated in Fig. 7.

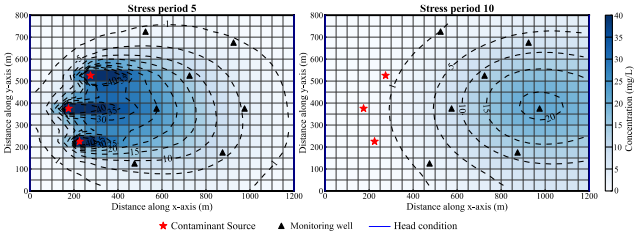


**Figure 7.** Distribution of contaminant plume in the 5th and 10th SPs of Case 2.

Compared with Case 1, Case 2 presents a significantly higher level of complexity for surrogate modelling and optimization. The number of discrete variables associated with source locations increases from 2 to 6, and the total number of unknown parameters rises from 10 to 24 due to the introduction of additional sources and their time-varying release fluxes.

### 4.3 Case 3

This case study is designed as a realistic numerical experiment based on the hydrogeological conditions of a mining area in Henan Province, China. The study area covers approximately 2.67 × 3 km. According to exploration-stage geological archives and field investigations, the aquifer is conceptualized as a single-layer unconfined system composed mainly of weathered and fractured granite, with an average saturated thickness of about 30 m. The underlying fresh granite is considered impermeable and therefore forms the basal boundary of the model. The groundwater flow system is represented by a two-dimensional single-layer numerical model. In plan view, the model domain is discretized using a structured grid with a uniform cell size of



Deleted: ¶

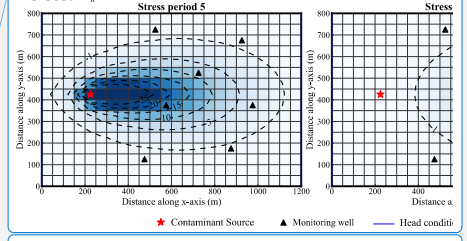


Deleted: :

Formatted: Font: Not Bold

Formatted: Font: Not Bold

Deleted: :

Formatted: Font: Not Bold

Formatted: Font: Not Bold

Deleted: As shown in Fig. 8, the

$30m \times 30m$, and the irregular outer boundary is represented by active and inactive cells, as shown in Fig. 8. The rivers along the western and eastern margins are treated as constant-head boundaries, whereas the northern and southern margins are specified as no-flow boundaries because they are bounded by relatively intact, low-permeability fresh granite. Groundwater recharge occurs primarily through vertical infiltration of precipitation and is represented using an average annual precipitation of 650 mm and a recharge coefficient of 0.12. To capture spatial heterogeneity, the aquifer is divided into four hydraulic conductivity zones based on the exploration-stage geological archives: Zone I corresponds to alluvial sand and gravel near the riverbanks, Zones II and III represent highly weathered and moderately weathered granite, respectively, and Zone IV represents a localized tectonic fracture zone. The main hydrogeological parameters adopted in the model are summarized in Table 2.

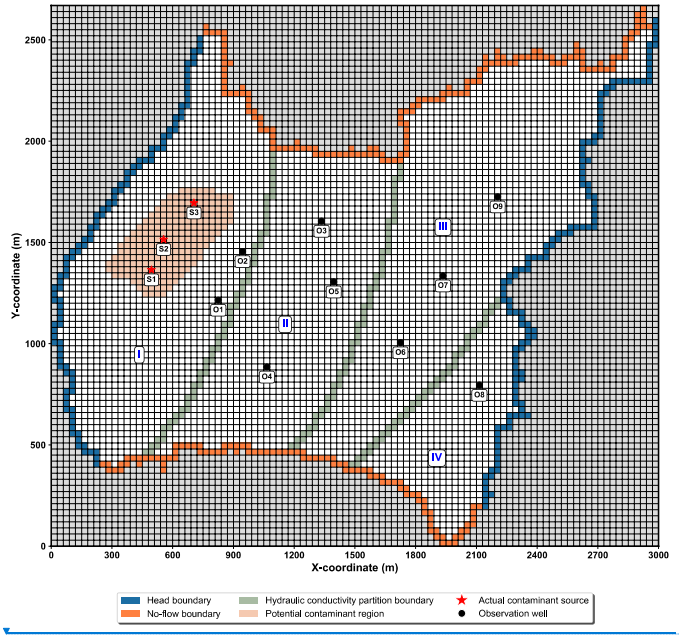


**Figure 8** Overview of the research region in Case 3.

A potential contaminant source region is delineated, as highlighted in pink in Fig. 8. Field investigations identify three waste-ore deposits ($S_1, S_2, S_3$) within this region. These sources continuously release contaminants into the groundwater during the first five stress periods (out of a total of ten). Nine observation wells are distributed across the study area to monitor contaminant migration, and Fig. 9 illustrates the observed temporal concentration variations over the stress periods.

**Table 2.** Basic settings of Case 3.



**Deleted:** on

**Deleted:** sides

**Deleted:** conceptualized

**Deleted:** while

**Deleted:** edges, dominated by

**Deleted:** with negligible

**Deleted:** or discharge, are represented as no-flow boundaries. The aquifer is further

**Deleted:**

**Deleted:** , denoted as

**Deleted:** $I$, $II$, $III$, and $IV$. The basic

**Deleted:** of

**Deleted:** aquifer

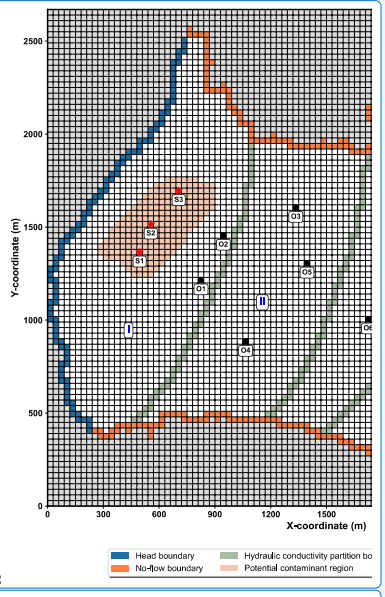


**Deleted:**

**Deleted:** :

**Formatted:** Font: Not Bold

**Formatted:** Font: Not Bold

| Name | Value or range |
|---|---|
| Hydraulic conductivity of Zone I, $K_I$, $m/day$ | $15.0 - 35.0$ |
| Hydraulic conductivity of Zone II, $K_{II}$, $m/day$ | $10.0 - 25.0$ |
| Hydraulic conductivity of Zone III, $K_{III}$, $m/day$ | $5.0 - 15.0$ |
| Hydraulic conductivity of Zone IV, $K_{IV}$, $m/day$ | $20.0 - 45.0$ |
| Porosity, $\theta$ | 0.3 |
| Longitudinal dispersity, $\alpha_L$, $m$ | 40.0 |
| Transverse dispersity, $\alpha_T$, $m$ | 11.0 |
| Saturated thickness, $b$, $m$ | 30.0 |
| Effective recharge rate, R, $m/day$ | $2.14 \times 10^{-4}$ |
| Hydraulic head of the left boundary, $H_1$, $m$ | 97.4 |
| Hydraulic head of the right boundary, $H_2$, $m$ | 83.1 |

In summary, the parameters to be identified include: (a) Hydrogeological parameters: The hydraulic conductivity ($K_1$, $K_2$, $K_3$, $K_4$); (b) Source locations ($SI_i$ and $SJ_i$, $i = 1, 2, 3$) and their release fluxes ($S_iP_t$, $i = 1, 2, 3$ and $t = 1\ to\ 5$ ), with the value of each flux bounded between 0 and 100 $kg/day$. Their actual values are listed in Table S3.

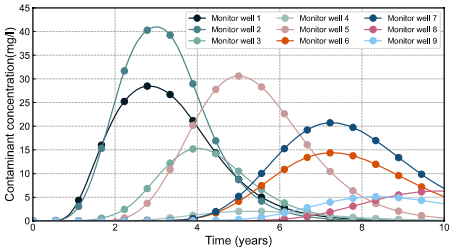


**Figure 9.** Observed concentrations at monitor wells in Case 3.

## 5 Comparison of surrogate models

### 5.1 Experiment setup

This study employs four commonly used surrogate models to investigate their performance in predicting the discrepancy between observed and simulated data for a given set of solutions: a. Kriging; b. Gaussian Process (GP); c. Support Vector Regression (SVR); d. Radial Basis Function (RBF).

To ensure a fair comparison, all surrogate models are constructed using UQPyL on a computer equipped with 12th Gen Intel(R) Core (TM) i5-12490F CPU, and 32.0 GB of RAM. For model configurations, based our preliminary experiments (Table S4), the Kriging model uses a Gaussian correlation function, whereas GP and RBF adopt Gaussian and Cubic kernels, respectively. All remaining hyperparameters are kept at their default settings in UQPyL.

For sample generation, Latin Hypercube Sampling (LHS) is used in Cases 1-3 to produce a set of parameter samples, which are subsequently input into the groundwater models to obtain contaminant concentrations. For each sample, the RMSE between the simulated and observed concentrations at all monitoring wells is calculated. RMSE is selected here because it

Deleted: :
Formatted: Font: Not Bold
Deleted: kernel
Deleted: radial
Deleted: cubic

provides a steeper and more informative gradient, which is advantageous for optimization. The generated parameter sets and their corresponding RMSE values constitute the full input-output datasets.

To evaluate model performance, four training datasets, denoted as DS1-DS4 with sample sizes of 100, 200, 300, and 500, respectively, are constructed. An independent set of 50 samples is generated for testing.

### 5.2 Evaluation of surrogate models

As described earlier, SA-CSA-TS constructs individual surrogate models for each monitoring well, and the corresponding outputs are summed to derive an ensemble objective value for optimization. To evaluate the effectiveness of this approach, we first examine the ensemble prediction performance of four surrogate models across Cases 1-3, based on the coefficient of determination ($R^2$). The results are summarized in Table 3.

**Table 3** Ensemble prediction performance of four surrogate models

| Case | Surrogate | Dataset | | | |
|---|---|---|---|---|---|
| | | DS1 | DS2 | DS3 | DS4 |
| Case 1 | KRG | 0.73 | 0.80 | 0.87 | 0.89 |
| | GP | 0.68 | 0.78 | 0.90 | 0.91 |
| | SVR | 0.46 | 0.54 | 0.72 | 0.75 |
| | RBF | 0.81 | 0.88 | 0.95 | 0.95 |
| Case 2 | KRG | 0.60 | 0.71 | 0.83 | 0.83 |
| | GP | 0.55 | 0.74 | 0.84 | 0.85 |
| | SVR | 0.35 | 0.47 | 0.62 | 0.64 |
| | RBF | 0.71 | 0.85 | 0.91 | 0.91 |
| Case 3 | KRG | 0.53 | 0.68 | 0.77 | 0.79 |
| | GP | 0.45 | 0.65 | 0.80 | 0.81 |
| | SVR | 0.30 | 0.37 | 0.46 | 0.48 |
| | RBF | 0.68 | 0.83 | 0.88 | 0.90 |

Across all datasets (DS1-DS4) and all three cases, RBF clearly delivers the most stable and accurate ensemble predictions. KRG and GP achieve acceptable accuracy, whereas SVR consistently performs the weakest. All models benefit from increasing training data. In comparison, RBF demonstrates a superior sensitivity to data enrichment, aligning well with the iterative reconstruction strategy of SA-CSA-TS. In Case 3, the prediction task becomes significantly more challenging due to more complex hydrogeological conditions, leading to lower $R^2$ values for all models. However, RBF still maintains robust predictive capability.

Based on the ensemble results, Cases 2 and 3 under dataset DS3 are selected for detailed surrogate evaluation at the individual monitoring wells. These two cases represent more challenging prediction scenarios. In addition, DS3 provides a sufficiently informative training set, yielding a clear performance improvement over DS2, while the additional gain from DS3 to DS4 is marginal. Figure 10 illustrates the prediction performance for Case 2 using DS3. Accuracy varies substantially across monitoring wells, primarily due to the spatial distribution of the contaminant plume. Wells 1, 2, and 5 are located within the main plume body, where steep and highly nonlinear concentration gradients dominate. Consequently, all surrogate models except RBF show marked reductions in $R^2$ at these locations. In contrast, Wells 6 and 7 lie far from the plume centre, where

Deleted: :

Formatted: Font: Not Bold

Deleted:

Formatted: Font: Not Bold

concentration gradients are smooth, enabling all models to reach their highest performance. A similar trend is observed in Case 3 (see Fig. 11). Wells situated in high-gradient zones (e.g., Wells 1, 2, 3, and 5) pose greater challenges, leading to noticeable performance declines for SVR, GP, and KRG. In contrast, RBF consistently maintains strong performance across all monitoring wells.

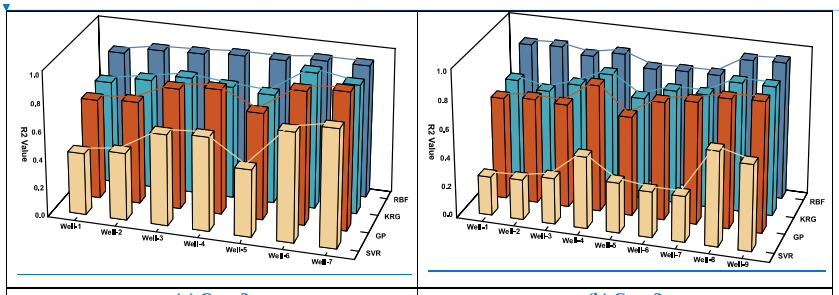


(a) Case 2 (b) Case 3

**Figure 10.** Prediction performance of surrogate models under dataset DS3 for two test cases: (a) Case 2 and (b) Case 3.

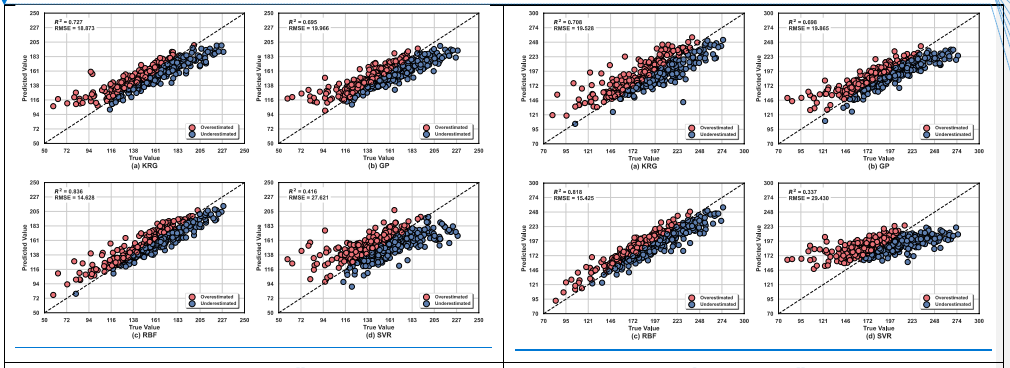


(a) Case 2, Well-1 (b) Case 3, Well-5

**Figure 11.** Sample-wise predicted versus true values of surrogate models for two representative cases: (a) Case 2, Well-1, and (b) Case 3, Well-5. In each subfigure, the four models are KRG, GP, RBF, and SVR.

Figure 11 present the sample-wise predicted values at representative locations: Well 1 for Case 2 and Well 5 for Case 3. In both scenarios, RBF achieves the highest $R^2$ and lowest RMSE, followed by KRG, GP, and SVR. In Case 3, SVR fails to capture the nonlinearity of contaminant concentrations, with its predictions collapsing into a narrow range. For optimization applications, high fidelity in the low-value region of the response is particularly important, as deviations in this domain can significantly affect the quality of the optimal solution. RBF provides more stable and accurate predictions in these low-value zones, further reinforcing its reliability as a surrogate model for optimization.



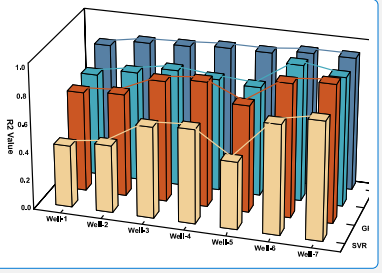


**Deleted:**

**Deleted:** :

**Deleted:** for Case 2

**Formatted:** Font: Not Bold

**Formatted:** Font: Not Bold

**Deleted:** the

**Formatted:** Font: Not Bold

**Formatted:** Font: Not Bold

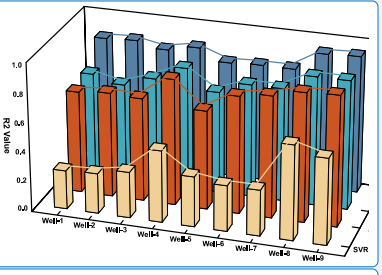


**Deleted:**

**Deleted:** : **Prediction performance**

**Deleted:** **Case 3 under the dataset DS3**

**Deleted:** Figures 12 and 13

In addition to prediction accuracy, the computational cost of training is a critical consideration for SA-CSA-TS, which involves iterative surrogate reconstruction. Theoretically, GP and KRG are computationally intensive with a complexity of $O(k \cdot N^3)$, where $k$ denotes the number of iterations required by the construction algorithm. In contrast, RBF and SVR offer higher computational efficiency, with complexities of $O(N^3)$ and $O(N^2) \sim O(N^3)$, respectively. This theoretical advantage is further supported by empirical results obtained using UQPyL on dataset DS4. In terms of actual training time, GP and KRG require approximately 1 s and 4 s, whereas RBF and SVR significantly reduce the cost to 0.22 s and 0.01 s.

In summary, RBF overcomes the precision limitations of SVR while avoiding the computational inefficiencies associated with KRG and GP. It thus provides the best balance between accuracy and efficiency, making it the most suitable surrogate model for the proposed SA-CSA-TS framework.

## 6 Optimization

### 6.1 Experiment setup

This section aims to investigate the performance of SA-CSA-TS in GCSI. For comparison, three additional optimization algorithms are considered: Genetic Algorithm (GA), Cooperative Search Algorithm (CSA) and SA-CSA. GA is widely used as a benchmark, whereas CSA represents a state-of-the-art method in recent years. SA-CSA is included to isolate and assess the contributions of the multi-chain framework and the Tabu Search. All algorithms are implemented within UQPyL to ensure a consistent and fair computational environment.

For the standard evolutionary algorithms (GA and CSA), the maximum number of simulations ($FE_{max}$) and the population size $N_p$ are set to 20,000 and 100. For GA, the user-defined parameters $p_c$, $\eta_c$, $p_m$, $\eta_m$ are set to 1, 20, $1/D$, 20, respectively, where $D$ denotes the dimensionality of the problem. For CSA, the parameters are set as $\alpha = 0.10$, $\beta = 0.15$, and $M = 3$.

For surrogate-assisted algorithms (SA-CSA-TS and SA-CSA), the RBF model is employed. The $FE_{max}$ is reduced to 2,000, as surrogate models enable efficient optimization with substantially fewer exact evaluations. Based on the results summarized in Table 3, the number of initial samples $N_I$ for surrogate construction is set to 300. For SA-CSA-TS, the number of chains is set to $K = 10$.

For Cases 1-3, the optimization problem is formulated as:

$$minimize: f = \sum_{m=1}^{M}\left(\sqrt{\frac{\sum_{t=1}^{T}(S_m^t - O_m^t)^2}{T}}\right) \quad (8)$$

$$subject\ to: LB \le \{H, K, SI, SJ, SP\} \le UB$$

where $S_m^t$ and $O_m^t$ represent the simulated and observed concentrations at the $m$-th monitoring well in stress period $t$, respectively. $LB$ and $UB$ are the lower and upper bounds of parameters to be estimated.

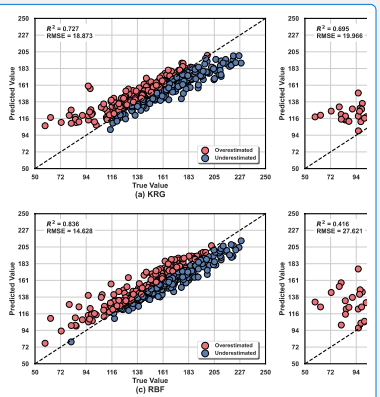


**Deleted:**

**Figure 12: Sample-wise predicted values of surrogate models in Case 2, Well-1¶**

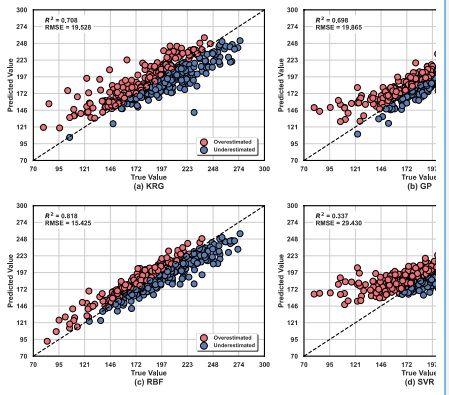


**Figure. 13 Sample-wise predicted values of surrogate models in Case 3, Well-5¶**

**Deleted:** 10

**Deleted:**

## 6.2 Optimization Results

### 6.2.1 Case 1

Figure 12a presents the convergence curves of the four algorithms in Case 1. SA-CSA-TS achieves the best objective value (0.35) within only 2,000 simulation runs, outperforming CSA, GA, and SA-CSA. As listed in Table 4, while all algorithms achieve satisfactory calibration for hydrogeological parameters, SA-CSA-TS is the only algorithm that consistently identifies the true source location $(5, 9)$ and release fluxes. This discrepancy highlights that the primary bottleneck lies in the discrete source search, where the proposed two-stage framework with Tabu Search effectively prevents the search chains from becoming trapped in local basins. Moreover, relative to conventional optimization approaches, the surrogate-assisted framework significantly reduces computational cost while maintaining high-quality solutions.

**Table 4** Optimization results of all algorithms in Case 1.

| Algorithms | Location $(SI, SJ)$ | Hydrogeological parameters | | | Release fluxes (kg/day) | | | | | Objective value |
|---|---|---|---|---|---|---|---|---|---|---|
| | | $H_1$ | $H_2$ | $K$ | $S_1P_1$ | $S_1P_2$ | $S_1P_3$ | $S_1P_4$ | $S_1P_5$ | |
| SA-CSA-TS | （5, 9） | 42.3 (0.9%) | 35.1 (0.5%) | 18.3 (1.1%) | 20.7 (3.3%) | 51.7 (1.0%) | 13.1 (3.0%) | 41.6 (2.2%) | 23.8 (3.9%) | 0.35 |
| SA-CSA | (4, 10) | 43.2 (1.2%) | 35.7 (1.1%) | 17.8 (1.7%) | 19.1 (8.9%) | 49.6 (4.7%) | 12.2 (6.4%) | 43.5 (8.8%) | 21.6 (2.1%) | 11.38 |
| GA | （6, 8） | 42.4 (0.7%) | 34.7 (1.7%) | 18.5 (1.7%) | 19.6 (6.8%) | 50.4 (3.0%) | 11.7 (9.8%) | 36.7 (8.2%) | 19.0 (13.6%) | 10.37 |
| CSA | （3, 7） | 43.7 (2.3%) | 35.9 (1.7%) | 18.2 (0.6%) | 19.9 (5.3%) | 52.3 (0.7%) | 12.5 (3.5%) | 42.3 (5.8%) | 20.9 (5.1%) | 9.19 |

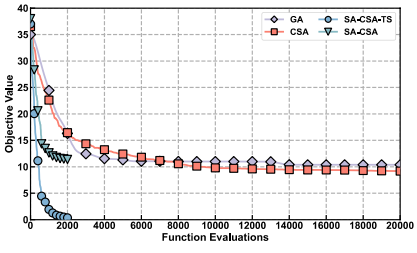


(a) Case1

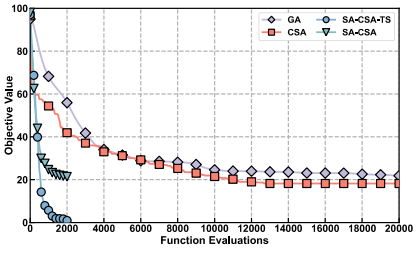


(b) Case2

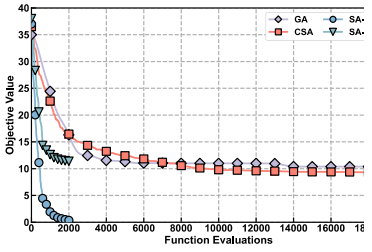


**Deleted:**
**Figure 14: Convergence curves of all algorithms in Case 1¶**

**Deleted:** 14

**Deleted:** :

**Formatted:** Font: Not Bold

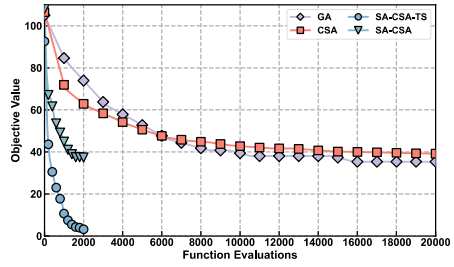


**(c) Case3**

**Figure 12.** Convergence curves of four algorithms for three cases: (a) Case 1, (b) Case 2, and (c) Case 3.

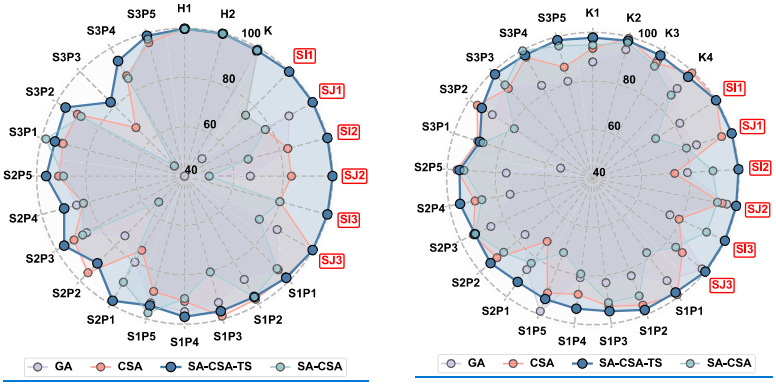


**(a) Case1** **(b) Case2**

**Figure 13.** Radar chart comparing the optimal solutions obtained by four algorithms: (a) Case1 and (b) Case2.

### 6.2.2 Case 2

Compared to Case 1, Case 2 involves three contaminant sources and therefore requires more parameters to be identified. Figure 12b presents the convergence behaviour of all algorithms. SA-CSA-TS achieves the best objective value (1.29), followed by CSA (18.23), SA-CSA (21.38) and GA (22.85). SA-CSA-TS also converges much more rapidly, stabilizing within the first 1,500 simulation runs.

Figure 13a compares the optimal solutions obtained by all algorithms. Higher radial values indicate more accurate estimates, with 100% denoting a perfect match to the true values. SA-CSA-TS encloses the largest area in the radar chart, indicating the highest overall estimation accuracy. While all algorithms provide satisfactory estimates of hydrogeological parameters, only SA-CSA-TS correctly identifies the three contaminant source locations (highlighted in red in Figure 13a).

**Deleted:** 15

**Deleted:** 16

**Deleted:** Fig. 16

Other algorithms exhibit noticeable deviations. Moreover, these incorrect source locations are accompanied by inaccurate release rates, suggesting that location errors are compensated by adjustments to other parameters, leading the search into local optima. Overall, with the assistance of surrogate models and Tabu Search, SA-CSA-TS demonstrates a strong ability to avoid such local traps and to accurately resolve the multi-source identification problem under this more complex scenario.

#### 6.2.3 Case 3

Case 3 presents the most challenging optimization landscape due to the increased number of parameters and scenario complexity. As illustrated in Figure 12c, the surrogate-assisted algorithms maintain a distinct efficiency advantage. In particular, SA-CSA-TS rapidly converges to the best solution within 2,000 simulations, whereas GA and CSA stagnate at significantly higher objective values.

Figure 13b details the identification accuracy for specific parameters. Consistent with previous cases, all algorithms estimate the hydrogeological parameters ($K_1$-$K_4$) with acceptable accuracy. However, a sharp performance divergence is observed in the source-related parameters: only SA-CSA-TS maintains high accuracy for the location variables ($SI$, $SJ$), while other algorithms exhibit substantial deviations. This failure to pinpoint source locations explains the stagnation observed in the other methods. Overall, Case 3 confirms that surrogate models effectively reduce computational cost, and that the multi-chain framework is indispensable for ensuring robustness and avoiding local optima in practical problems.

## 7 Discussion

### 7.1 Effects of surrogate models

Surrogate models are incorporated into SA-CSA-TS to alleviate the computational burden of high-fidelity simulations. Figure 14 breaks down the runtime of all algorithms across the three cases into simulation time (blue) and algorithm time (red). It is evident that the simulation cost overwhelmingly dominates the total runtime. Although surrogate-assisted methods introduce a slight overhead for model construction and updating, this cost is negligible compared to the time savings achieved by reducing high-fidelity evaluations. Specifically, in three case studies, SA-CSA-TS reduces the total runtime by approximately 85-88%, compared to the GA and CSA. This result confirms that the efficiency advantage of the surrogate-assisted framework becomes increasingly pronounced as the problem complexity grows.

Given the negligible overhead of surrogate modelling, the effect of the iterative reconstruction strategy is further examined. Figure 15 tracks the evolution of prediction accuracy ($R^2$) of surrogate models on a validation set during optimization. In Case 1, the accuracy remains high and stable. In contrast, Cases 2 and 3 exhibit noticeable fluctuations. These oscillations are not indicators of failure but rather reflect the algorithm's active exploration of underrepresented regions. Driven by the Tabu Search mechanism, the optimizer periodically escapes local basins and enters unexplored areas where the surrogate model initially has lower accuracy. However, the subsequent recovery of $R^2$ values confirms that the surrogate model



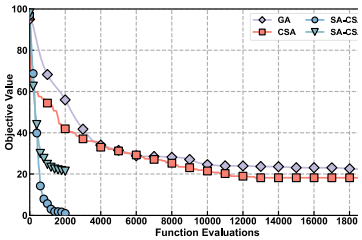


Deleted:
**Figure 15: Convergence curves of all algorithms in Case 2¶**

Deleted: Fig. 17

Deleted: 18

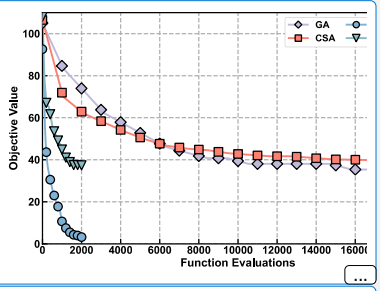


Deleted:

Deleted: 19

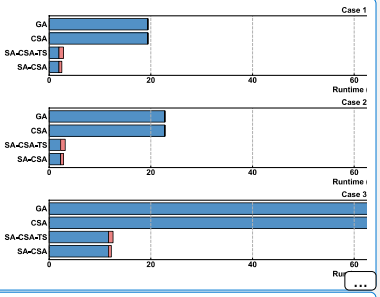


Deleted:

Deleted: 20

successfully adapts to these new regions. Crucially, this dynamic updating process prevents the convergence stagnation observed in the other algorithms, ensuring that the search remains robust even in complex landscapes.

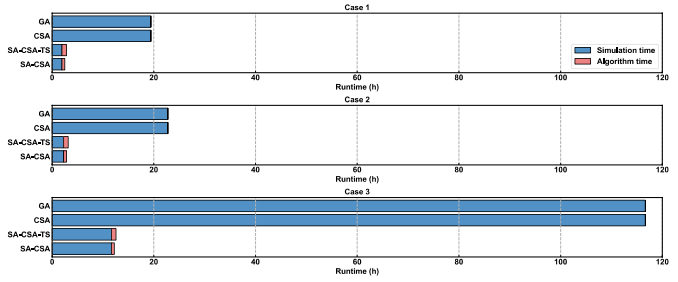


**Figure 14.** Runtime breakdown of all algorithms across three cases.

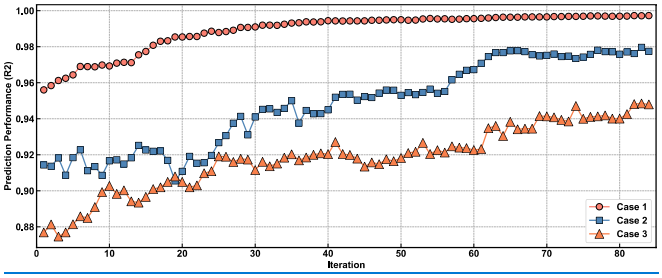


**Figure 15.** Evolution of the prediction accuracy of the RBF model on the validation set during the optimization process.

### 7.2 Effects of the multi-chain framework

Groundwater contaminant source identification is an inherently multi-modal optimization problem, where inaccurate location estimates may easily trap algorithms in inferior local solutions. As observed in Figs. 14, 15, and 17, GA, CSA and SA-CSA frequently exhibited instability and stagnation. This failure is largely attributed to their reliance on a single search population or trajectory, which lacks the mechanism to escape local basins. In contrast, SA-CSA-TS successfully identified the source information in all three cases. To understand this mechanism, we examine the behaviour of the proposed multi-chain framework.

Figure 16 depicts the search-frequency maps of candidate source locations by SA-CSA-TS for Case 1 and Case 2. In both scenarios, the true source locations (marked by red bars) correspond to the highest visit frequencies (red circles), indicating that the majority of chains consistently converge toward the correct region. Notably, the surrounding cells also exhibit high visit frequencies. This phenomenon confirms the parameter-compensation effect, where spatial inaccuracies are temporarily

Deleted: 21

balanced by adjustments in release fluxes or hydraulic conductivity. This "equifinality" trap explains why conventional algorithms often stagnate near, but not exactly at, the true source. Furthermore, Case 2 displays more dispersed secondary hotspots than Case 1, reflecting a more rugged landscape with stronger compensability. Despite this complexity, the proposed framework successfully concentrates the search effort on the true location, demonstrating robust global convergence. Further improvement may be achieved in future work by incorporating optimal monitoring well placement to provide stronger spatial constraints and further reduce the parameter-compensation effect.

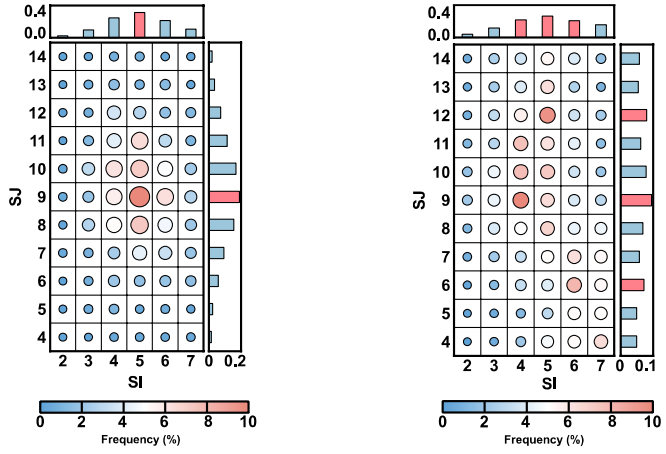


**Figure 16.** Search-frequency maps of candidate source locations obtained by the multi-chain framework in (a) Case 1 and (b) Case 2. The red bars indicate the true source locations.

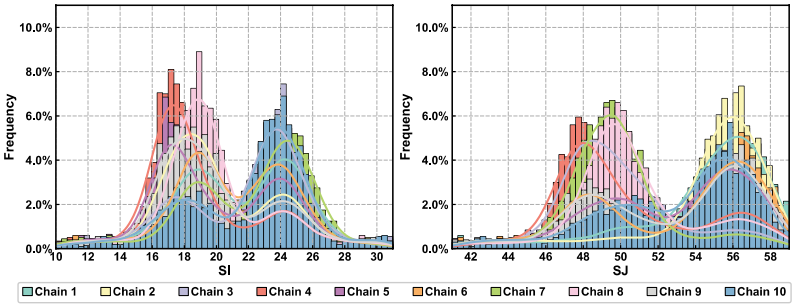


**Figure 17.** Distribution of search trajectories across ten chains for source coordinates in Case 3. The fitted curves highlight the multi-modal nature of the search landscape.

Deleted: 21:

Formatted: Font: Not Bold

Deleted: 22:

Formatted: Font: Not Bold

Figure 17 provides a deeper insight by analysing the distribution of search trajectories across ten independent chains in Case 3. The histograms for the source coordinates ($SI$ and $SJ$) reveal a distinct multi-modal distribution, confirming the existence of multiple local optima. While the majority of chains converge to the primary peak (the true source), a few chains (e.g., Chains 1, 2, and 10) are entrapped in secondary peaks. Therefore, if a single-chain method (like standard GA or CSA) is used, and it happens to follow the trajectory of Chain 1, the identification would fail entirely. However, the multi-chain framework mitigates this risk by exploring multiple basins simultaneously. This collective intelligence allows the algorithm to filter out local optima and stabilize estimates around the true global solution, effectively overcoming the equifinality and multi-modality challenges that hinder conventional single-population methods.

### 7.3 Robustness analysis

To evaluate the robustness of SA-CSA-TS under data uncertainty, additional experiments are conducted based on three case studies. Random Gaussian noise with varying levels (0.5%, 1%, and 2%) is superimposed on the noise-free observation data, following the equation:

$$C_{obs}^{*} = C_{true} \cdot (1 + \delta \cdot \xi) \quad (9)$$

where $C_{obs}^{*}$ and $C_{true}$ denote the noisy and noise-free observations, respectively; $\delta$ denotes the noise level; and $\xi$ is a random number following the standard normal distribution $N(0, 1)$.

Figure 18 illustrates the Average Relative Errors (ARE) for the three cases under these noise levels. A clear trend is observed where the identification error increases marginally with the noise intensity. Specifically, for Case 1, the ARE rises from 1.59% (noise-free) to 3.09% (2% noise). For the more complex scenarios in Cases 2 and 3, the errors start at approximately 3.7–3.8% and increase to roughly 4.5% under the maximum noise level. Despite these increases, the average errors for all cases consistently remain below 5%, indicating that the proposed method maintains high performance without significant degradation when observation data is subject to measurement noise.

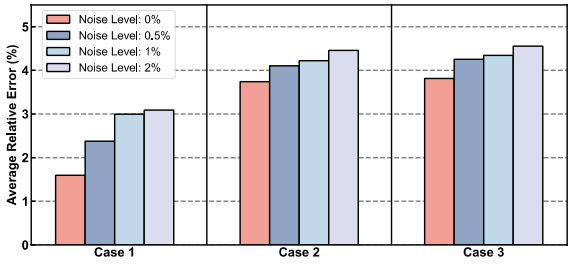


**Figure 18.** Comparison of average relative errors for three cases under different noise levels.

Tables S5-S7 provide the specific identification results in three cases. Notably, the discrete source locations match the true values exactly across all noise levels. As for continuous variables, the hydrogeological parameters show only slight



Deleted: 22

Formatted: Right

Deleted: 23

Deleted: S4-S6

fluctuations. In comparison, the source release parameters exhibit relatively larger variations. This phenomenon is largely attributed to the complementary effects between different stress periods or among multiple sources, where slight deviations in one parameter may compensate for another. Despite this, the overall errors remain within an acceptable range, confirming the robustness of SA-CSA-TS against data uncertainty.

### 7.4 Limitations

Despite the promising performance and robustness of SA-CSA-TS, some limitations should be further discussed. First, this study evaluates the proposed algorithm only using two-dimensional groundwater systems. The search strategy of SA-CSA-TS, however, is guided by the difference between simulated and observed responses at monitoring locations, rather than by the assumption tied to a specific groundwater model dimensionality. This gives the SA-CSA-TS potential for extension to three-dimensional groundwater models. Nevertheless, its applicability to three-dimensional flow and hydrodynamic dispersion systems has not yet been demonstrated in this study. Furthermore, an increase in vertical resolution (depth layers) not only raises the computational cost of groundwater simulation but also poses a challenge to the predictive fidelity of the surrogate model in complex cases, which should be confirmed through further investigation. Second, while the robustness analysis demonstrated resilience against Gaussian noise, real-world field conditions often involve more complex uncertainties. These include sparse monitoring networks, systematic measurement biases, and structural model errors. Therefore, future work should focus on testing SA-CSA-TS in three-dimensional systems and under combined uncertainty sources, in order to establish its robustness and reliability for complex groundwater inverse problems.

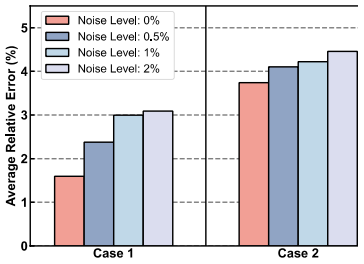


**Deleted:**
**Figure: 23 Comparison of average relative errors for three cases under different noise levels¶**
¶
¶

## 8 Conclusions

This study proposes a multi-chain surrogate-assisted hybrid optimization algorithm, SA-CSA-TS, to address the challenges of prohibitive computational costs and multi-modal complexity in GCSI. The algorithm incorporates three key innovations. First, surrogate models are embedded to alleviate the computational burden, while continuous iterative updates ensure reliable optimization guidance. Second, a multi-chain synergistic learning framework enables the exchange of evaluated samples among chains, enhancing data diversity and preventing premature convergence caused by limited local information. Third, a two-stage sequential strategy is employed where CSA conducts global exploration and TS performs neighbourhood refinement guided by a shared tabu list, effectively balancing exploration and exploitation.

Through three illustrative case studies, the applicability of different surrogate models and the overall performance of the proposed algorithm were systematically investigated. Results indicate that the Radial Basis Function (RBF) offers the best balance of stability and accuracy, particularly excelling in fitting low-value regions, making it the optimal surrogate for this framework. Comparative experiments with four algorithms (SA-CSA-TS, GA, CSA, and SA-CSA) highlight the superior robustness and accuracy of the proposed framework. While the benchmark algorithms frequently stagnate in local optima due to the parameter-compensation effect, SA-CSA-TS successfully identifies the true contaminant source parameters by

leveraging multi-chain cooperation to escape local entrapment. Furthermore, the algorithm achieves a computational cost reduction of approximately 85-88% across the three cases, proving it to be both a precise and efficient tool for GCSI. Future work will focus on extending the framework to three-dimensional and more heterogeneous aquifer systems, with particular emphasis on assessing surrogate predictive fidelity and computational scalability in complex cases to support practical applications. In addition, the integration of surface–groundwater interactions and multi-source data (e.g., satellite-derived observations) will be explored to provide additional constraints for parameter identification.

Deleted: this

Deleted: highly

Deleted: aquifers and exploring parallel computing techniques

Deleted: further enhance its applicability in real-time emergency response

## Code and Data availability

The codes and case studies used in this work are available at https://doi.org/10.5281/zenodo.17862863 (Wu, 2025) and maintained at the GitHub repository (https://github.com/smasky/SA-CSA-TS). All numerical experiments are carried out using the UQPyL platform, which is available at http://www.uq-pyl.com (or https://github.com/smasky/UQPyL).

## CRediT author statement

Mengtian Wu: Methodology, Software, Writing – original draft, Writing – review & editing, Funding acquisition; Xuan Huang: Methodology, Software; Pengcheng Xu: Methodology, Software; Xu Yang: Software; Han Chen: Methodology, Software; Jin Xu: Methodology; Qingyun Duan: Conceptualization, Methodology, Funding acquisition, Project administration


## Acknowledgments

This study was supported by the Jiangsu Provincial Science and Technology Basic Research Program Youth Fund Project [grant number BK20241516], the National Natural Science Foundation of China [grant numbers 42101046 and W2431029], the National Key R&D Program of China [grant number 2021YFC3201102], and the Key Scientific and Technological Project of the Ministry of Water Resources of the P.R.C. [grant number SKS-2022001].

**Declaration of competing interest**

The authors declare that they have no known competing financial interests or personal relationships that could have appeared to influence the work reported in this paper.

**References**


Agbotui, P. Y., Firouzbehi, F., Medici, G. 2025. Review of effective porosity in sandstone aquifers: insights for representation of contaminant transport. Sustainability, 17(14), 6469.

Asher, M.J., Croke, B.F.W., Jakeman, A.J., Peeters, L.J.M., 2015. A review of surrogate models and their application to groundwater modeling: SURROGATES OF GROUNDWATER MODELS. Water Resour. Res. 51, 5957–5973. https://doi.org/10.1002/2015wr016967

Ayvaz, M.T., Elci, A., 2018. Identification of the optimum groundwater quality monitoring network using a genetic algorithm based optimization approach. J. Hydrol. 563, 1078–1091. https://doi.org/10.1016/j.jhydrol.2018.06.006

Bai, T., Tahmasebi, P., 2022. Characterization of groundwater contamination: a transformer-based deep learning model. Adv. Water Resour. 164, 104217. https://doi.org/10.1016/j.advwatres.2022.104217

Bakker, M., Post, V., Langevin, C.D., Hughes, J.D., White, J.T., Starn, J.J., Fienen, M.N., 2016. Scripting MODFLOW Model Development Using Python and FloPy. Groundwater 54, 733–739. https://doi.org/10.1111/gwat.12413

Broomhead, D.S., Lowe, D., 1988. Multivariable functional interpolation and adaptive networks. Complex Systems 2, 321–355.

Chang, C.-C., Lin, C.-J., 2011. LIBSVM: a library for support vector machines. ACM Trans. Intell. Syst. Technol. 2, 27:1-27:27. https://doi.org/10.1145/1961189.1961199

Chang, Z., Lu, W., Wang, Z., 2021. A differential evolutionary markov chain algorithm with ensemble smoother initial point selection for the identification of groundwater contaminant sources. J. Hydrol. 603, 126918. https://doi.org/10.1016/j.jhydrol.2021.126918

Delshad, M., Pope, G.A., Sepehrnoori, K., 1996. A compositional simulator for modeling surfactant enhanced aquifer remediation, 1 formulation. J. Contam. Hydrol. 23, 303–327. https://doi.org/10.1016/0169-7722(95)00106-9

Feng, Z., Niu, W., Liu, S., 2021. Cooperation search algorithm: A novel metaheuristic evolutionary intelligence algorithm for numerical optimization and engineering optimization problems. Appl. Soft Comput. 98, 106734. https://doi.org/10.1016/j.asoc.2020.106734

Gorelick, S.M., Zheng, C., 2015. Global change and the groundwater management challenge. Water Resour. Res. 51, 3031–3051. https://doi.org/10.1002/2014WR016825

Guneshwor, L., Eldho, T.I., Kumar, A.V., 2018. Identification of groundwater contamination sources using meshfree RPCM simulation and particle swarm optimization. Water Resour. Manage. 32, 1517–1538. https://doi.org/10.1007/s11269-017-1885-1

Harbaugh, A.W., 2005. MODFLOW-2005, the US Geological Survey modular groundwater model-the groundwater flow process. Cent. Integr. Data Anal. Wis. Sci. Cent.

Hou, Z., Lu, W., 2018. Comparative study of surrogate models for groundwater contamination source identification at DNAPL-contaminated sites. Hydrogeol. J. 26, 923–932. https://doi.org/10.1007/s10040-017-1690-1

Hughes, J.D., Langevin, C.D., Banta, E.R., 2017. Documentation for the MODFLOW 6 framework (USGS Numbered Series No. 6-A57), Documentation for the MODFLOW 6 framework, Techniques and Methods. U.S. Geological Survey, Reston, VA. https://doi.org/10.3133/tm6A57

Jha, M., Datta, B., 2013. Three-dimensional groundwater contamination source identification using adaptive simulated annealing. J. Hydrol. Eng. 18, 307–317. https://doi.org/10.1061/(ASCE)HE.1943-5584.0000624

Li, J., Lu, W., Fan, Y., 2021. Groundwater pollution sources identification based on hybrid homotopy-genetic algorithm and simulation optimization. Environ. Eng. Sci. 38, 777–788. https://doi.org/10.1089/ees.2020.0117

Li, P., Karunanidhi, D., Subramani, T., Srinivasamoorthy, K., 2021. Sources and consequences of groundwater contamination. Arch. Environ. Contam. Toxicol. 80, 1–10. https://doi.org/10.1007/s00244-020-00805-z

Li, Y., Lu, W., Pan, Z., Wang, Z., Dong, G., 2023. Simultaneous identification of groundwater contaminant source and hydraulic parameters based on multilayer perceptron and flying foxes optimization. Environ. Sci. Pollut. Res. 30, 78933–78947. https://doi.org/10.1007/s11356-023-27574-1

Lophaven, S.N., Nielsen, H.B., Søndergaard, J., 2002. DACE: a Matlab kriging toolbox. Citeseer.

Luo, C., Wang, X., Xu, Y.J., Jia, S., Liu, Z., Mao, B., Lv, Q., Ji, X., Rong, Y., Dai, Y., 2025. Synergistic identification of hydrogeological parameters and pollution source information for groundwater point and areal source contamination based on machine learning surrogate–artificial hummingbird algorithm. Hydrol. Earth Syst. Sci. 29, 5719–5736. https://doi.org/10.5194/hess-29-5719-2025

Mahar, P.S., Datta, B., 2001. Optimal identification of ground-water pollution sources and parameter estimation. J. Water Resour. Plan. Manag.-asce 127, 20–29. https://doi.org/10.1061/(ASCE)0733-9496(2001)127:1(20)

Meenal, M., Eldho, T.I., 2012. Simulation-optimization model for groundwater contamination remediation using meshfree point collocation method and particle swarm optimization. Sadhana-acad. Proc. Eng. Sci. 37, 351–369. https://doi.org/10.1007/s12046-012-0086-0

Mirghani, B.Y., Mahinthakumar, K.G., Tryby, M.E., Ranjithan, R.S., Zechman, E.M., 2009. A parallel evolutionary strategy based simulation-optimization approach for solving groundwater source identification problems. Adv. Water Resour. 32, 1373–1385. https://doi.org/10.1016/j.advwatres.2009.06.001

Ouyang, Q., Lu, W., Miao, T., Deng, W., Jiang, C., Luo, J., 2017. Application of ensemble surrogates and adaptive sequential sampling to optimal groundwater remediation design at DNAPLs-contaminated sites. J. Contam. Hydrol. 207, 31–38. https://doi.org/10.1016/j.jconhyd.2017.10.007

Pan, Z., Lu, W., Wang, H., Bai, Y., 2023. Groundwater contaminant source identification based on an ensemble learning search framework associated with an auto xgboost surrogate. Environ. Modell. Software 159, 105588. https://doi.org/10.1016/j.envsoft.2022.105588

Rasmussen, C.E., Williams, C.K.I., 2006a. Gaussian Processes for Machine Learning. MIT Press, Cambridge, MA, USA.

Rasmussen, C.E., Williams, C.K.I., 2006b. Gaussian processes for machine learning, Adaptive computation and machine learning. MIT Press, Cambridge, Mass.

Razavi, S., Tolson, B.A., Burn, D.H., 2012a. Numerical assessment of metamodelling strategies in computationally intensive optimization. Environ. Modell. Software 34, 67–86. https://doi.org/10.1016/j.envsoft.2011.09.010

Razavi, S., Tolson, B.A., Burn, D.H., 2012b. Review of surrogate modeling in water resources. Water Resour. Res. 48, W07401. https://doi.org/10.1029/2011wr011527

Singh, A., 2015. Review: computer-based models for managing the water-resource problems of irrigated agriculture. Hydrogeol. J. 23, 1217–1227. https://doi.org/10.1007/s10040-015-1270-1

Singh, R.M., Datta, B., 2006. Identification of groundwater pollution sources using GA-based linked simulation optimization model. J. Hydrol. Eng. 11, 101–109. https://doi.org/10.1061/(ASCE)1084-0699(2006)11:2(101)

Song, J., Yang, Y., Chen, G., Sun, X., Lin, J., Wu, Jianfeng, Wu, Jichun, 2019. Surrogate assisted multi-objective robust optimization for groundwater monitoring network design. J. Hydrol. 577, 123994. https://doi.org/10.1016/j.jhydrol.2019.123994

Song, J., Yang, Y., Wu, Jianfeng, Wu, Jichun, Sun, X., Lin, J., 2018. Adaptive surrogate model based multiobjective optimization for coastal aquifer management. J. Hydrol. 561, 98–111. https://doi.org/10.1016/j.jhydrol.2018.03.063

Swetha, K., Eldho, T.I., Singh, L.G., Kumar, A.V., 2025. Groundwater contaminant source identification using swarm intelligence-based simulation optimization models. Environ. Sci. Pollut. Res. Int. 32, 1626–1639. https://doi.org/10.1007/s11356-024-35850-x

Wang, J.L., Lin, Y.H., Lin, M.D., 2015. Application of heuristic algorithms on groundwater pumping source identification problems, in: 2015 IEEE International Conference on Industrial Engineering and Engineering Management (Ieem). Presented at the IEEE International Conference on Industrial Engineering and Engineering Management (IEEM), IEEE, New York, pp. 858–862.

Wang, Z., Lu, W., Chang, Z., Zhang, T., 2024. Joint identification of groundwater pollution source information, model parameters, and boundary conditions based on a novel ES-MDA with a wheel battle strategy. J. Hydrol. 636, 131320. https://doi.org/10.1016/j.jhydrol.2024.131320

Wu, M., Wang, L., Xu, J., Hu, P., Xu, P., 2022a. Adaptive surrogate-assisted multi-objective evolutionary algorithm using an efficient infill technique. Swarm Evol. Comput. 75, 101170. https://doi.org/10.1016/j.swevo.2022.101170

Wu, M., Wang, L., Xu, J., Wang, Z., Hu, P., Tang, H., 2022b. Multiobjective ensemble surrogate-based optimization algorithm for groundwater optimization designs. J. Hydrol. 612, 128159. https://doi.org/10.1016/j.jhydrol.2022.128159

Wu, M. 2025. SA-CSA-TS: A multi-chain surrogate-assisted hybrid optimization algorithm combining CSA and TS. Zenodo. https://doi.org/10.5281/zenodo.17862863.

Xing, Z., Qu, R., Zhao, Y., Fu, Q., Ji, Y., Lu, W., 2019. Identifying the release history of a groundwater contaminant source based on an ensemble surrogate model. J. Hydrol. 572, 501–516. https://doi.org/10.1016/j.jhydrol.2019.03.020

Yin, J., Tsai, F.T.-C., 2020. Bayesian set pair analysis and machine learning based ensemble surrogates for optimal multi-aquifer system remediation design. J. Hydrol. 580, 124280. https://doi.org/10.1016/j.jhydrol.2019.124280

Zhao, Y., Lu, W., Xiao, C., 2016. A kriging surrogate model coupled in simulation-optimization approach for identifying release history of groundwater sources. J. Contam. Hydrol. 185, 51–60. https://doi.org/10.1016/j.jconhyd.2016.01.004

Zheng, C., Wang, P.P., 1999. MT3DMS: a modular three-dimensional multispecies transport model for simulation of advection, dispersion, and chemical reactions of contaminants in groundwater systems; documentation and user's guide.

Zhu, L., Lu, W., Luo, C., Xu, Y., Wang, Z., 2024. An ensemble optimizer with a stacking ensemble surrogate model for identification of groundwater contamination source. J. Contam. Hydrol. 267, 104437. https://doi.org/10.1016/j.jconhyd.2024.104437